

Advances in the Direct Spectral Estimation of Aeroacoustic Sources Using Continuous-Scan Phased Arrays

David Morata* and Dimitri Papamoschou.†
University of California, Irvine, Irvine, CA, 92607

The paper presents improvements to the methodology for the direct estimation of the spatio-spectral distribution of an acoustic source from microphone measurements that comprise fixed and continuously scanning sensors. The signals from the scanning sensors are non-stationary due to the time-varying source-sensor distance and the traversing of an acoustic field with spatially varying statistics. Quasi-stationarity is sought by dividing the signals into blocks and applying of a frequency-dependent window within each block. The effects of the block distribution and width of the window on the acoustic source images are analyzed and guidelines are developed for optimal block sizes. The methodology is applied to acoustic fields emitted by a subsonic jet in isolation and surrounded by a plate in shielding and reflection orientations. The experimental setup consists of a microphone phased array with one scanning and multiple fixed sensors. The ability of the continuous-scan paradigm, coupled with the improved signal division, to provide high-definition noise source maps is demonstrated.

Nomenclature

a	=	speed of sound
c_λ	=	fraction of acoustic wavelength traveled
c_{cov}	=	coverage of Gaussian window width
D	=	jet diameter
f	=	cyclic frequency
F_s	=	sampling rate
K	=	number of blocks
ℓ	=	source-sensor distance
N_B	=	size of the block (in samples)
N_T	=	size of the signal (in samples)
N_{FFT}	=	size of Fast Fourier Transform
p	=	pressure fluctuation
S	=	number of segments in a block
t	=	time
T	=	duration of the block
U	=	fully-expanded jet velocity
V	=	sensor speed
x	=	axial coordinate
y	=	transverse coordinate
δ	=	width of Gaussian window
ϵ	=	error
θ	=	polar angle relative to jet axis
λ	=	acoustic wavelength
ξ	=	axial coordinate
ψ	=	coherence-based source distribution
σ_s	=	segment overlap
σ_B	=	block overlap
τ	=	source-sensor time
ω	=	angular frequency

*Graduate Student Researcher, Mechanical and Aerospace Engineering, dmorata@uci.edu, Member AIAA.

†Professor, Mechanical and Aerospace Engineering, dpapamos@uci.edu, Fellow AIAA.

ω' = Doppler-shifted frequency
 ω'' = frequency of spectral oscillation

Subscripts

f = fixed sensor
 k = block index
 m, n = sensor indices
 s = scanning sensor

Acronyms

DAS = Delay and Sum
 DSE = Direct Spectral Estimation
 DSEV = Direct Spectral Estimation with Variable Block Division
 FFT = Fast Fourier Transform
 SPL = Sound Pressure Level
 WVS = Wigner-Ville spectrum
 XWVS = cross Wigner-Ville spectrum

I. Introduction

Noise source imaging using a collection of microphone measurements has become an indispensable tool of aeroacoustic investigations. Traditional beamforming generates noise source maps by “steering” the microphone array to a region of interest. The resulting image is a convolution between the modeled source distribution and the array point spread function. To improve the spatial resolution of the image, and reject the sidelobes that are inherent in the point spread function, various deconvolution approaches have been developed [1–4]. An alternative to the steering approach is direct estimation of the the source distribution via least-square minimization of the difference between the modeled and the measured pressure statistics. These statistics are typically in the forms of the cross-spectral or coherence matrices. The required inversion can be performed by a variety of methods, including Bayesian estimation [5–7]. The direct estimation approach has been shown to provide results comparable or superior to those obtained via the deconvolution method [5, 8].

Recently there has been increasing interest in microphone arrays in which one or more of the sensors are traversing along prescribed paths in a continuous motion. For a fixed sensor count, the continuous-scan paradigm can improve the spatial resolution and the overall quality of of the noise source maps. It has found applications in near-field holography [9, 10], order tracking [11] and beamforming [5, 8, 12]. Sensor motion introduces non-stationarity in the signal statistics that requires special processing techniques. A methodology for the direct spectral estimation of acoustic sources from microphone measurements involving fixed and scanning sensors was presented in Ref. [5]. The technique used the Wigner-Ville spectrum to quantify the non-stationarity of the signal arising from the scanning sensors. Suppression of the non-stationarity involved the division of the signal into blocks and the application of a frequency-dependent window within each block.

The goal of the present study is optimization of the signal treatment for handling non-stationary signals in the direct spectral estimation method. Geometric effects, spatial resolution, spectral accuracy, and adequacy of samples within each block are considered in the formulation of criteria for optimal block size and block overlap within frequency ranges. The optimized methodology is applied to the acoustic field emitted by a subsonic jet in isolation and surrounded by a rectangular plate in shielding and reflection orientations.

II. Inverse Acoustic Methodology for Continuous-Scan Phased Arrays

This section outlines the key features of the direct spectral estimation method with scanning sensors of Ref. [5]. The application is a turbulent jet whose noise source distribution is approximated by a line of uncorrelated monopoles, as depicted in Fig. 1, where ξ is the source coordinate. We allow for directional sources and denote the source distribution $q(\xi, \theta, t)$, with θ the polar angle measured from location ξ . A series of microphone sensors is deployed,

each sensor traversing with a speed V_m along a path parallel to the source line. Assuming spherical spreading in a quiescent medium with uniform speed of sound a , and allowing for slow scan with $V_m \ll a$, the pressure recorded by sensor m is [5]

$$p_m(t) = \int_{\mathcal{L}} \frac{1}{\ell_m(\xi, t)} q[\xi, \theta_m(\xi, t), t - \tau_m(\xi, t)] d\xi \quad (1)$$

where

$$\tau_m(\xi, t) = \frac{\ell_m(\xi, t)}{a} \quad (2)$$

is the source-sensor propagation time and $\ell_m(\xi, t)$ is the source-sensor distance. The integration along the source axis ξ is limited to the region of interest \mathcal{L} where significant noise sources are expected. Non-stationarity arises from the time variation of $\ell_m(\xi, t)$ as well as the traversing of an acoustic field with spatially-varying statistics.

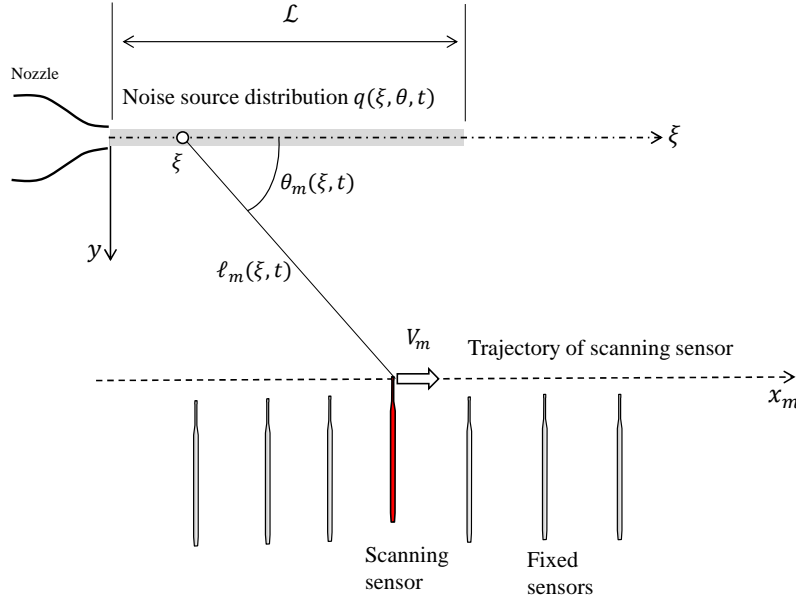


Fig. 1 Line source distribution and geometry of scanning sensor.

The Wigner-Ville spectrum (WVS) was identified as a robust method for spectral analysis of non-stationary signals. The WVS is defined as the Fourier Transform of the symmetric autocorrelation (or cross-correlation for the XWVS). For stationary processes, the ensemble average is replaced with the time average invoking the principle of ergodicity. For a non-stationary process, this is not possible unless the signal is quasi-stationary. Quasi-stationary is achieved by segmenting the signal into smaller blocks. Considering block k with center time t_k and duration T , subscript mk denotes the quantities associated with sensor m at $t = t_k$. The following approximations are made:

$$\begin{aligned} \tau_m(\xi, t) &\approx \tau_{mk}(\xi) + \left(\frac{\partial \tau_m(\xi, t)}{\partial t} \right)_{t=t_k} (t - t_k) \\ \ell_m(\xi, t) &\approx \ell_{mk}(\xi) \\ \theta_m(\xi, t) &\approx \theta_{mk} \end{aligned} \quad (3)$$

The validity of the approximations of Eq. 3 drives the definition of an upper bound for the block size, to be detailed in Section IV.

The most serious effect of non-stationarity is on the correlation of signals from sensors having a relative velocity. At frequency ω the XVWS of sensor signals $p_m(t)$ and $p_n(t)$ is affected by two parameters linked to the motion of the sensors: a Doppler-shifted frequency

$$\omega'_{mnk} = \omega \left[1 + \frac{1}{2} \left(\frac{V_m}{a} \cos \theta_{mk}(\xi) + \frac{V_n}{a} \cos \theta_{nk}(x) \right) \right] \quad (4)$$

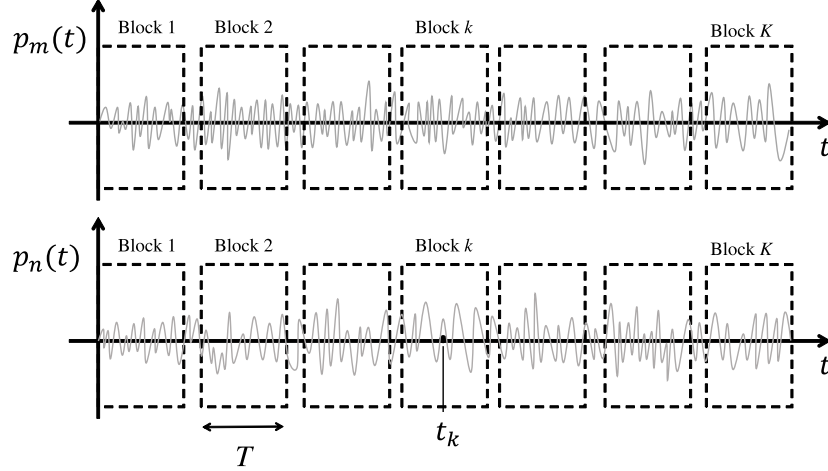


Fig. 2 Illustration of division of the signal into K quasi-stationary blocks.

and a frequency of oscillation of the entire spectrum

$$\omega''_{mnk} = \omega \left[\frac{V_n}{a} \cos \theta_{nk}(x) - \frac{V_m}{a} \cos \theta_{mk}(\xi) \right] \quad (5)$$

where x is a running coordinate along ξ . Minimization of ω''_{mnk} to near-zero value is essential for accurate imaging and constitutes the strongest challenge in the signal processing. Considering only one sensor scanning with velocity V_m , suppression of the oscillation requires

$$V_m T \ll \frac{\lambda}{\pi \cos \theta_{\mu k}} \quad (6)$$

where T is the duration of the block and λ is the acoustic wavelength. This motivates the implementation of a Gaussian frequency-dependent window[5] of the signal within each block to meet the above criterion. The width of the window δ satisfies

$$V_m \delta = c_\lambda \lambda = c_\lambda \frac{a}{f} \quad (7)$$

where c_λ is the fraction of the acoustic wavelength that the sensor traverses in time δ . Typical value for c_λ is 0.2. Meeting the requirement of Eq. 7 while retaining critical information of the signal requires a careful balance of block size, block overlap, and size of the Fourier transform used to compute the spectrum. This is at the heart of the new signal processing procedures presented here.

Following the development in Ref. [5] the coherence of the acoustic field for block k is

$$\gamma_{mnk}(\omega) = \int_{\mathcal{L}} Z_{mnk}(x, \omega) \psi(x, \omega) dx \quad (8)$$

where $\psi(x, \omega)$ is the *coherence-based* noise source distribution and

$$Z_{mnk}(x_0, \omega) = \exp \left\{ i \omega'_{mnk} [\tau_{nk}(x_0) - \tau_{mk}(x_0)] \right\} \quad (9)$$

is the array response matrix which describes the modeled coherence of the acoustic field for a point source at $x = x_0$. Equation 8 represents a model for the coherence of the acoustic field and constitutes the basis for the solutions that will follow. The diagonal terms of satisfy

$$\int_{\mathcal{L}} \psi(x, \omega) dx = 1 \quad (10)$$

This is an important property of the coherence-based noise source that should be kept in mind when examining its spatial distribution. Equation 8 is inverted here using a Bayesian estimation method [5].

III. Block Division

The block division introduced in the previous section has direct impact on the quality of the noise source maps and requires a thorough evaluation. Criteria to determine the number of blocks and their size are formulated in terms of the geometry of the microphone array, the source directivity, the spectral estimation algorithm, and the width of the frequency-dependent window. Guidance for the optimal number of blocks, block size, and block overlap will be developed. We only consider a uniform signal division (equal block sizes) for each frequency range of interest.

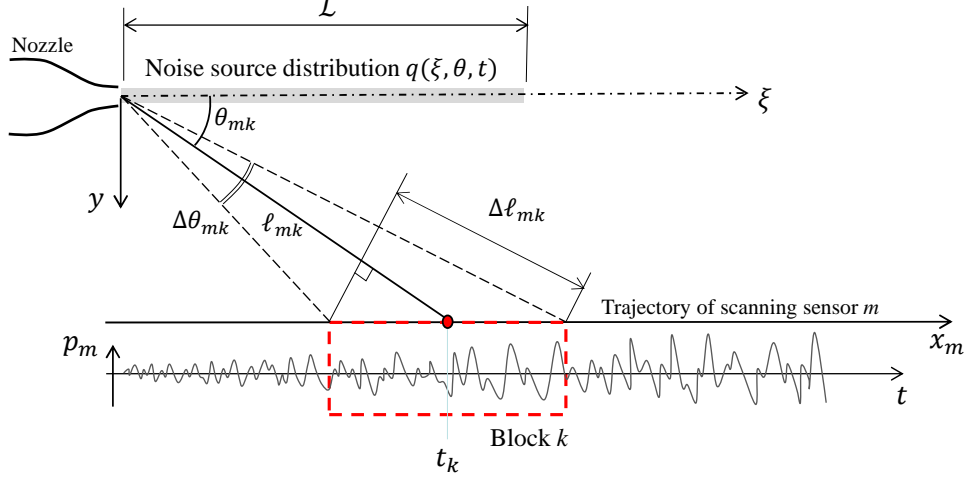


Fig. 3 Distance and angle variations associated with the length of a signal block.

A. Maximum Block Size

The evaluation of the maximum block size is based on the quasi-stationary approximations of Eq. 3. Referring to Fig. 3, in the analysis that follows the origin of the source is placed at the origin $(\xi, y) = (0, 0)$ for simplicity. This is valid when the sensors are in the geometric far field; otherwise, the steps presented below would need to be extended to various locations in the source region.

The first concern is the validity $\ell_m(\xi, t) \approx \ell_{mk}(\xi)$ in Eq. 3. Considering a given block k for sensor m , this involves the variation of the source-sensor distance within the block and can be quantified as

$$\epsilon_{\ell, mk} = \frac{|\Delta \ell_{mk}|}{\ell_{mk}} \quad (11)$$

where ℓ_{mk} is the source-sensor distance at the center of the block and $\Delta \ell_{mk}$ is the variation of this distance across the block, as illustrated in Fig. 3.

The second concern is the approximation $\theta_m(\xi, t) \approx \theta_{mk}$. For a substantially omnidirectional acoustic field, this approximation is directly connected to Eq. 11 and can thus be made redundant. However, in a field with strong directivity, the directivity can overwhelm geometric effects and therefore the validity of this approximation needs to be evaluated separately. Considering a source with characteristic polar directivity Θ , the error is formulated as

$$\epsilon_{\theta, mk} = \frac{|\Delta \theta_{mk}|}{\Theta} \quad (12)$$

where $\Delta \theta_{mk}$ is the polar angle variation across the block, as indicated in Fig. 3. As an example, Fig. 4 plots the far-field narrowband spectra for a cold Mach 0.9 jet studied here at a number of polar angles θ . Near the angle of peak emission ($\theta = 30^\circ$) the spectrum varies as much as 3 dB for $\Delta \theta = 5^\circ$. In this case, we selected $\Theta = 0.0873 \text{ rad} = 5^\circ$.

To determine the maximum bound on the block size, first the error thresholds are set. In this study, we selected $\epsilon_{\ell, mk} = 0.01$ and $\epsilon_{\theta, mk} = 0.3$. The sensor's trajectory is discretized into fine increments $x_k, k = 1, \dots, M$ representing the location of the center of a block. For each x_k , the sample size N_k of the block determines its spatial extent through the sampling rate F_s and the sensor speed V_m , allowing calculation of the errors. N_k is increased from low value until

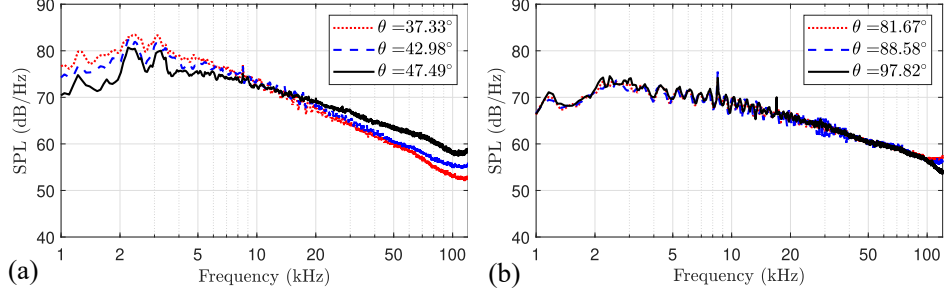


Fig. 4 Variation of narrowband SPL spectra with polar angle from the jet axis for a cold subsonic jet with $M = 0.9$ exit flow studied in this work. (a) Spectra near the direction of peak emission; (b) spectra near the broadside direction.

one of the error thresholds is exceeded; this sets the final value of N_k . Seeking a uniform block size, the maximum bound is set equal to the minimum value of the vector N_k , that is,

$$N_{B_{\max}} = \min(N_k, k = 1, \dots, M) \quad (13)$$

B. Minimum Block Size

The need to suppress the spectral oscillation frequency of Eq. 5 drives the processing towards small block sizes, particularly at high frequency. However, the block needs to contain sufficient samples to compute the auto- and cross-spectral densities accurately, the latter being strongly impacted by non-stationarity. This motivates the development of a criterion for the lower bound of the block size.

Consider signals $p_m(t)$ and $p_n(t)$ corresponding to the pressure recorded by a scanning sensor and a fixed sensor, respectively. The signals are divided into K overlapping or non-overlapping blocks, each one of them containing N_B samples. For each block, the cross-spectral density is estimated by (i) dividing each signal into S segments with overlap σ_s ; (ii) computing the Fast Fourier Transform (FFT) of the signals in each segment; (iii) multiplying appropriately the FFTs of the two signals within each segment; and (iv) averaging the results over the number of segments. In the last step, the accuracy and smoothness of the result improve with increasing S . The FFT algorithm requires that each segment contains $2N_{\text{FFT}}$ samples, where N_{FFT} is the size of the Fourier Transform. It is easy to show that the size of the block is related to the number of segments, segment overlap, and FFT size as follows:

$$N_B = 2N_{\text{FFT}} \left[(1 - \sigma_s)(S - 1) + 1 \right] \quad (14)$$

For fixed segment overlap and FFT size, the minimum size of the block is dependent on the smallest number of segments that allows for accurate spectral estimation. This is directly linked to the nature of the acoustic source as well as to the array geometry.

We propose a method to evaluate the accuracy of spectral estimation by using the narrowband sound pressure level (SPL) spectrum of the scanning sensor. The SPL is computed with fixed overlap, fixed N_{FFT} , and increasing number of segments S (thus increasing number of total samples) until the maximum bound, determined in the previous section, is reached. Denoting SPL_S and SPL_{S-1} the SPL computed with number of segments S and $S - 1$, respectively, the difference $\Delta\text{SPL}_S = \text{SPL}_S - \text{SPL}_{S-1}$ is plotted versus S for a number of frequencies. Figure 5 plots this relationship for the present jet and array geometry, with $N_{\text{FFT}} = 512$ and $\sigma_s = 0.5$. It is seen that ΔSPL_S undergoes strong oscillations when the number of segments is small. At around $S = 15$ the spectral estimation achieves an accuracy of ~ 0.3 dB. Beyond this value, improvement is very gradual. The envelope (dashed line) drawn in Fig. 5 provides guidance as to the minimum number of segments S_{\min} required for accurate spectral estimation. It is advisable to perform this analysis for various values of N_{FFT} , although in the present experiments the result was largely independent of N_{FFT} . From Eq. 14 the minimum size of the block becomes

$$N_{B_{\min}} = 2N_{\text{FFT}} \left[(1 - \sigma_s)(S_{\min} - 1) + 1 \right] \quad (15)$$

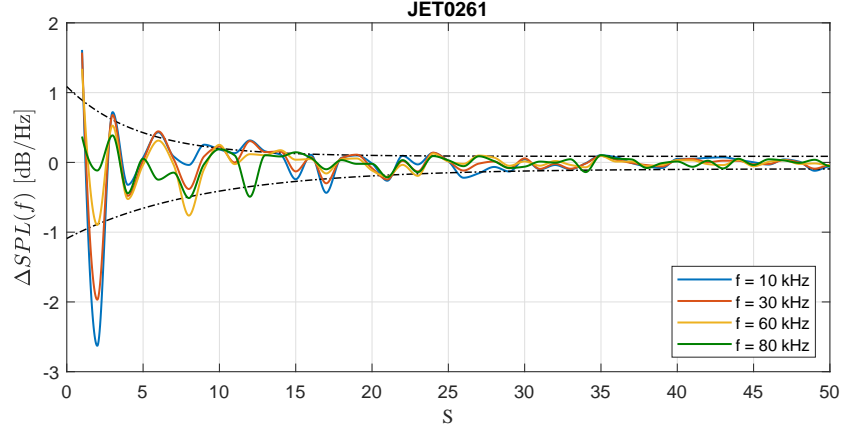


Fig. 5 Δ SPL computed with consecutive segment increases as a function of the number of segments.

C. Effect of the Frequency-Dependent Window

The Gaussian window associated with Eq. 7 has the form

$$g(t, \omega) = A(\omega) \exp \left\{ - \left[\frac{t}{\delta(\omega)} \right]^2 \right\} \quad (16)$$

where $\delta(\omega)$ is a time scale that declines with frequency (Eq. 7) and

$$A(\omega) = \left(\frac{2}{\pi} \right)^{1/4} \sqrt{\frac{T}{\delta(\omega)} \frac{1}{\operatorname{erf} \left(\frac{T}{\sqrt{2} \delta(\omega)} \right)}} \quad (17)$$

is an amplitude that makes the window energy-preserving [5]. Multiplication of the signal within each block by a frequency-dependent window produces an effective reduction of the block size, as illustrated in Fig. 6. The reduction can be severe at high frequency, meaning that a significant portion of the block is unused.

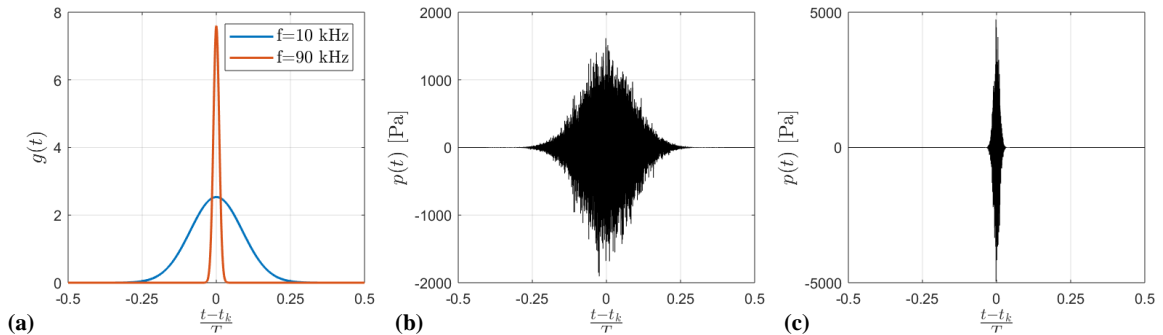


Fig. 6 Example of the frequency-dependent Gaussian window for frequencies of $f = 10$ kHz and $f = 90$ kHz. (a) Shape of the Gaussian envelope; (b) pressure signal multiplied by the Gaussian window for $f = 10$ kHz; (c) pressure signal multiplied by the Gaussian window for $f = 90$ kHz;

To limit the loss of information, we can consider maintaining the ratio T/δ constant. This would entail different block division for each frequency and therefore spectral estimation for each element of the frequency vector at prohibitive computational cost. It would also obviate the need for the Gaussian window, which allows efficient spectral estimation across the entire frequency vector. However, it will be shown that setting $T \sim \delta$ connects directly T to the size of the

FFT, which has a step-wise relation with frequency. In other words, the above relation becomes discrete and requires spectral estimation for only a small number of frequency ranges, typically four.

The window width must be adequately covered by the segments used in the spectral estimation. We require coverage of c_{cov} non-overlapping segments, meaning that

$$\delta = c_{\text{cov}} \Delta t_{\text{seg}}$$

where $\Delta t_{\text{seg}} = 2N_{\text{FFT}}/F_s$ is the duration of each segment. Accordingly,

$$T = 2 \frac{T}{\delta} c_{\text{cov}} \frac{N_{\text{FFT}}}{F_s}$$

Multiplying by F_s we obtain an additional upper bound on the block size, which we denote

$$N_{B_{\text{max}}}^* = 2 \frac{T}{\delta} c_{\text{cov}} N_{\text{FFT}} \quad (18)$$

The coverage requirement imposes the restriction [5]

$$N_{\text{FFT}} \leq \frac{1}{2} \frac{c_\lambda}{c_{\text{cov}}} \frac{a}{V_m} \frac{F_s}{f} \quad (19)$$

Because N_{FFT} must be a power of two, this entails discrete reduction of N_{FFT} with increasing frequency, and attendant discrete reduction of the block size.

For example, setting $T/\delta = 1.7$ ensures that the tails of the Gaussian filter reach 50% of the peak value at the ends of the block. For adequate coverage of δ , a reasonable selection is $c_{\text{cov}} = 5$. Then, Eq. 18 becomes

$$N_{B_{\text{max}}}^* = 17 N_{\text{FFT}}$$

Matching the lower and upper bounds given by Eqs. 15 and 18, respectively, allows determination of the segment overlap

$$\sigma_s = 1 - \frac{\frac{T}{\delta} c_{\text{cov}} - 1}{S_{\text{min}} - 1} \quad (20)$$

D. Number of Blocks and Block Overlap

Considering a signal with total number of samples N_T divided into blocks of size N_B and overlap σ_b , it is straightforward to derive that the number of blocks is

$$K = 1 + \frac{1 - \frac{N_B}{N_T}}{\frac{N_B}{N_T} (1 - \sigma_b)} \quad (21)$$

The ratio N_B/N_T is a dimensionless block size. The block overlap quantifies the repeated information contained in contiguous blocks. A large block overlap increases the total computation time as it increases the number of blocks without gaining new information. It is important to note that is a direct relation between the the number of blocks and the number of independent elements J of the coherence matrix, as presented in Ref. [5]:

$$J = M_f^2 - M_f + 1 + K M_s (M_s + 2M_f - 1) \quad (22)$$

where M_f and M_s are the number of fixed and scanning sensors, respectively. The size of J relates to the cost of computing the coherence matrix as well as the cost of inverting the integral of Eq. 8. On the other hand, a low block overlap combined with a large number of blocks might lead to small block size that violates the minimum bound previously discussed. In addition, low block overlap combined with a small number of blocks may result into large block size that compromises the spatial resolution of the method at high frequency, as will be discussed in the next section. It is thus reasonable to determine a range of block overlap that does not penalize the accuracy of the spectral estimation and avoids unnecessary computations while enhancing the spatial resolution of imaging. Here, we propose a range of block overlap between $\sigma_b = 0.1$ and $\sigma_b = 0.5$ that accounts for these considerations.

E. Optimal Signal Division

We summarize the guidance for signal division. There is a geometric criterion, Eq. 13, that sets an upper bound on block size, $N_{B_{\max}}$, for ensuring that the approximations of Eq. 3 are valid. The accuracy of spectral estimation imposes a lower bound, $N_{B_{\min}}$, formulated in Eq. 15. Prevention of information loss from the frequency-dependent window that filters each block requires an additional maximum bound, $N_{B_{\max}}^*$, defined by Eq. 18. Both $N_{B_{\min}}$ and $N_{B_{\max}}^*$ are directly proportional to the size of the FFT, N_{FFT} , used for spectral estimation, which has a step-wise declining relation with frequency.

The qualitative diagrams of Fig. 7 help explain these relationships. Figure 7a displays the trend of the block-size bounds versus N_{FFT} . $N_{B_{\max}}$ is invariant on N_{FFT} since it depends only on the array geometry and speed of the sensor. $N_{B_{\max}}^*$ and $N_{B_{\min}}$ are linear with N_{FFT} . The area bounded by $N_{B_{\max}}^*$, $N_{B_{\min}}$, and $N_{B_{\max}}$ (highlighted in green) represents optimal block sizes. The relation of N_{FFT} with frequency is sketched in Fig. 7b. It declines in step-ladder fashion with frequency following Eq. 19 and the requirement that N_{FFT} be an integer power of two. Figure Fig. 7c represents the combination of the trends in the previous figures, showing that $N_{B_{\max}}^*$ and $N_{B_{\min}}$ decline in discrete steps with increasing frequency. The green region again represents optimal block sizes. The sample size of the window width δF_s is a smooth function of frequency. So, while the block size experiences discrete changes, the smoothness of δ ensures that filtering is done in a continuous fashion with minimal loss of information.

It is possible to match $N_{B_{\max}}^*$ and $N_{B_{\min}}$ by setting the overlap of signal segmentation σ_s (used in spectral estimation) according to Eq. 20. This would result in the most efficient block division in terms of computational cost. Once the block sizes are set versus frequency, the number of blocks follows Eq. 21. If it turns out that $N_{B_{\max}}^* < N_{B_{\min}}$, and this cannot be fixed by reasonable settings of σ_s , it would imply that experimental parameters such as sensor speed and sampling frequency may need to be revised.

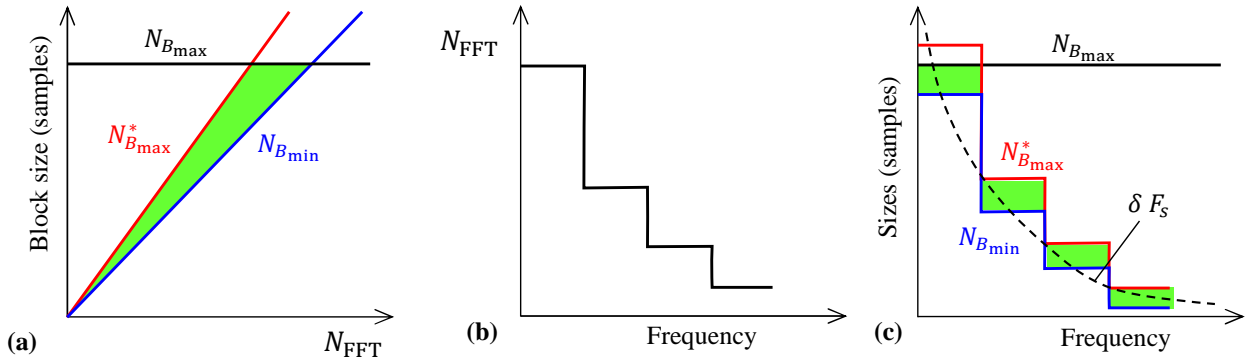


Fig. 7 Trends governing the determination of optimal block size. (a) Block-size bounds versus N_{FFT} ; (b) N_{FFT} relation with frequency; (c) Block-size bounds and Gaussian window width (in samples) versus frequency. Green regions indicates optimal block size.

IV. Experimental Setup

A. Phased Microphone Array

Noise measurements were conducted in the UCI Aeroacoustics Facility whose anechoic chamber is depicted in Fig. 8. The microphone array comprises twenty-four 1/8-inch condenser microphones (Brüel and Kjaer, Model 4138). The microphones are connected, in groups of four, to six conditioning amplifiers (Brüel and Kjaer, Model 2690-A-0S4). The outputs of the amplifiers are sampled simultaneously, at 250 kHz per channel, by three 8-channel multi-function data acquisition boards (National Instruments PCI-6143) installed in a PC with Intel i7-7700K quad-core processor. National Instruments Labview software is used to acquire the signals with a custom built program and user interface. Temperature and humidity are recorded inside the anechoic chamber to enable computation of atmospheric absorption and calculation of the exact speed of sound. The microphone signals were conditioned with a high-pass filter set at 350 Hz to remove any spurious noise. Narrowband sound pressure level (SPL) spectra were computed with $N_{\text{FFT}}=2048$

yielding a frequency resolution of 122 Hz. The spectra were corrected for microphone actuator response, microphone free field response and atmospheric absorption, thus resulting in lossless spectra. They are referenced to a radius of 0.305 m.

On the L-shaped holder of the fixed microphones, 12 microphones were arranged on the horizontal arm and 11 on the vertical arm. The scanning microphone was mounted on a linear traverse consisting of a belt drive (Igus ZLW-0630) powered by a servo motor (ClearPath MCPV). Its scan line was $\Delta y = 6$ mm above the line of the fixed sensors on the horizontal arm of the holder. Figure 9a plots the coordinates of the fixed sensors and initial location of the scanning sensor for the nominal array configuration on the horizontal arm (the coordinates of the sensors on the vertical arm are not included). A sparse array configuration, depicted in Fig. 9b, utilized the scanning sensor with only four fixed sensors on the horizontal arm and none on the vertical arm. The nominal array covered a polar angle sector $\theta = 19^\circ$ to 98° .

During microphone signal acquisition the servo was programmed to rotate at fixed revolutions per minute, moving the linear stage at constant speed of 75.94 mm/s with a stroke length of 900 mm. To avoid damage to the sensor, a smooth ramp up and ramp down of the sensor speed was programmed. The position of the traverse was monitored via the motor encoder and independently using a laser-based distance measurement device (SICK OD1000). A total of 3×10^6 samples were acquired for each channel corresponding to an acquisition time of 12 s. A frequency-dependent Gaussian window with $c_\lambda = 0.2$ was applied in the computation of the noise source maps.

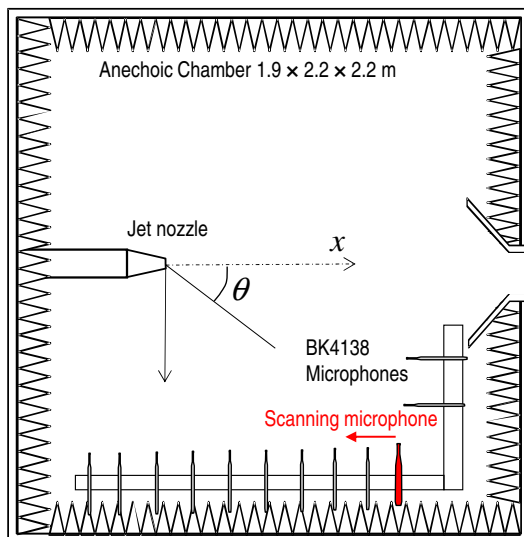


Fig. 8 Anechoic chamber and qualitative deployment of the microphones.

B. Signal Division

We present noise source maps computed obtained with three methods: Delay and sum (DAS); Direct Spectral Estimation (DSE) using uniform block division; and Direct Spectral Estimation using variable block division according the guidance developed in Section III. We will refer to the latter method as DSEV. For both DSE and DSEV, the integral of Eq. 8 was inverted using the Bayesian estimation approach of Ref. [5]. The DAS method used only fixed sensors with $N_{\text{FFT}} = 2048$, while DSE and DSEV utilized fixed and scanning sensors in the deployments shown in Fig. 9. Table 1 lists the block schedule and other relevant parameters for DSEV. DSE used the same N_{FFT} schedule as DSEV but with fixed $K = 48$, $N_B = 122880$, and $\sigma_B = 0.5$. For both DSE and DSEV, noise source maps are obtained by patching results at the various frequency ranges indicated.

C. Noise Sources

This study examined a jet source and its interaction with a shielding plate and a reflection plate. The jet issued from a convergent nozzle with exit diameter $D = 21.8$ mm. It was supplied by air at room temperature and pressure of

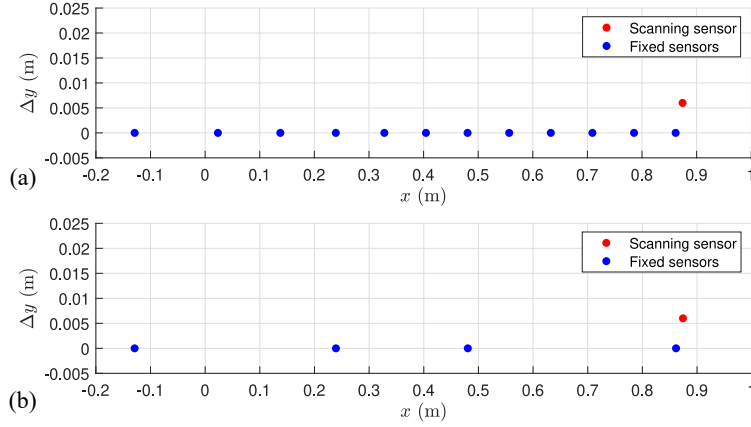


Fig. 9 Coordinates of fixed sensors on horizontal arm and initial position of scanning sensor for two array configurations: (a) nominal; (b) sparse.

Frequency Range (kHz)	N_{FFT}	N_B	T (s)	K	σ_B
0-25	2048	36000	0.144	166	0.50
25-50	1024	15000	0.060	399	0.50
50-70	512	8026	0.032	750	0.50
70-95	256	4080	0.016	1480	0.50

Table 1 Block division for DSEV method.

10 psig, producing an exhaust at Mach number $M = 0.9$ and velocity $U = 309$ m/s. The nozzle and microphone array are depicted in Fig. 10.

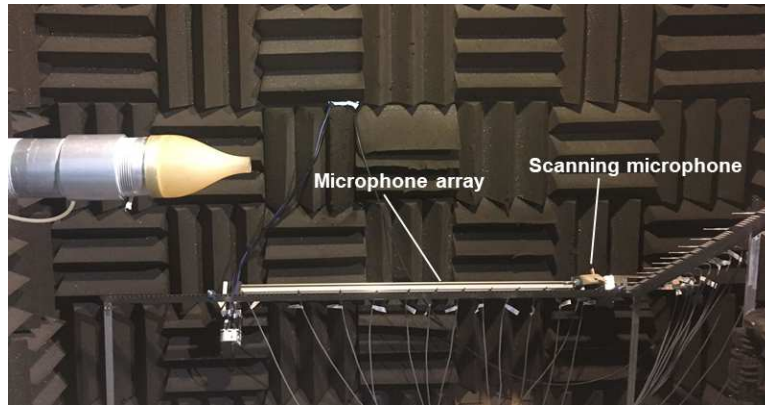


Fig. 10 Jet nozzle and microphone array.

A rectangular aluminum plate was integrated with the jet to study the effects of shielding and reflection. The plate had thickness of 2 mm, span of 610 mm, and chord length $c = 128$ mm. A schematic of the setup is depicted in Fig. 11. The vertical distance H from the jet axis to the plate was kept constant while the horizontal distance L of the trailing edge from the nozzle exit plane was varied according to Table 2. Rotation of the plate enabled shielding and reflection measurements. Images of the setup are depicted in Fig. 12. For the largest $L = 127$ mm, the trailing edge was positioned at an angle of 20° relative to the jet centerline, a value much larger than the spreading rate of the shear

layer (see, for example, Ref. [13]). Therefore, the jet was not scrubbing on the plate.

Experiment	L (mm)	H (mm)	Case
JET0261	-	-	Isolated
JET0221	101.6	45	Shielding
JET0231	127.0	45	Shielding
JET0251	101.6	45	Reflection
JET0241	127.0	45	Reflection

Table 2 Geometry of installed configurations.

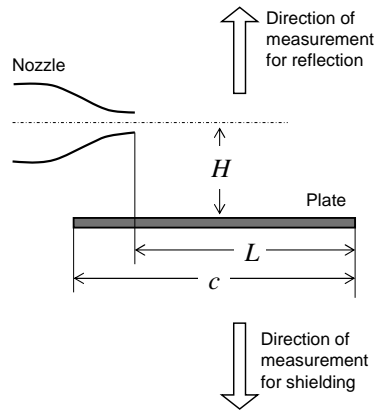


Fig. 11 Schematic of the nozzle integrated with plate.

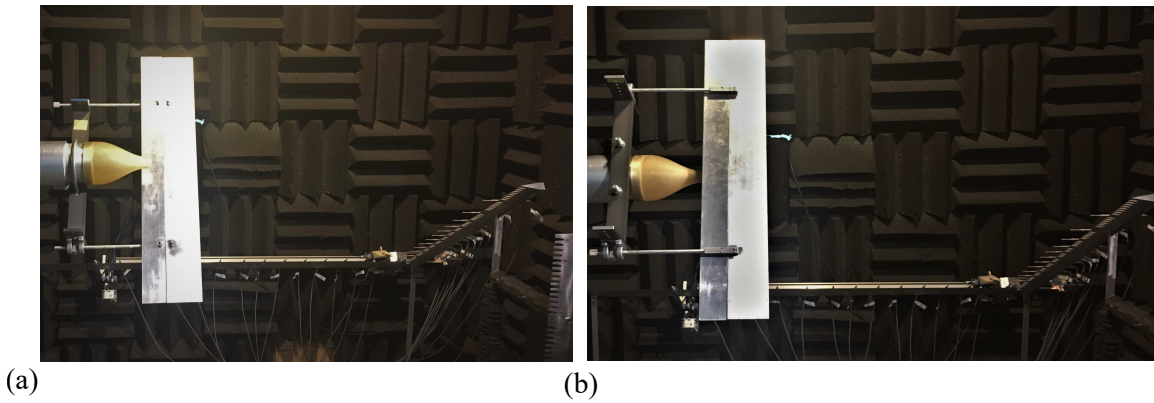


Fig. 12 Pictures of installed configuration with $L=101.6$ mm. (a) Shielding orientation; (b) reflection orientation.

V. Results

Acoustic results are first presented for the nominal array configuration of Fig. 9a, where all the available microphones were used. They are followed by results using the sparse array of Fig. 9b.

A. Isolated Jet

Figure 13 plots the lossless narrowband SPL spectra for the isolated jet, measured with the fixed microphones only, at various polar angles θ . The spectra are clearly directional with the turbulent mixing noise undergoing strong variations with polar angle. Figure 14 presents coherence-based noise source maps ($\psi(x, \omega)$ of Eq. 8) for the isolated jet, obtained with the DAS, DSE, and DSEV methods. The DAS map shows strong sidelobes and its the spatial resolution is very limited. The spatial features of the source, especially at the high frequencies, are smeared and distorted due to the sidelobes. The DSE map results in a more defined source with strong suppression of the sidelobes. The DSEV map shows increased resolution at high frequency and practically complete suppression of the sidelobes. Spectral peaks at low frequency are likely due to internal noise (see for example [14]) and are not relevant to these or subsequent results. The axial distribution of the source is in line with previous findings [15]: the peak noise source location for lowest frequencies extends significantly downstream and it moves closer to the nozzle exit as the frequency increases.

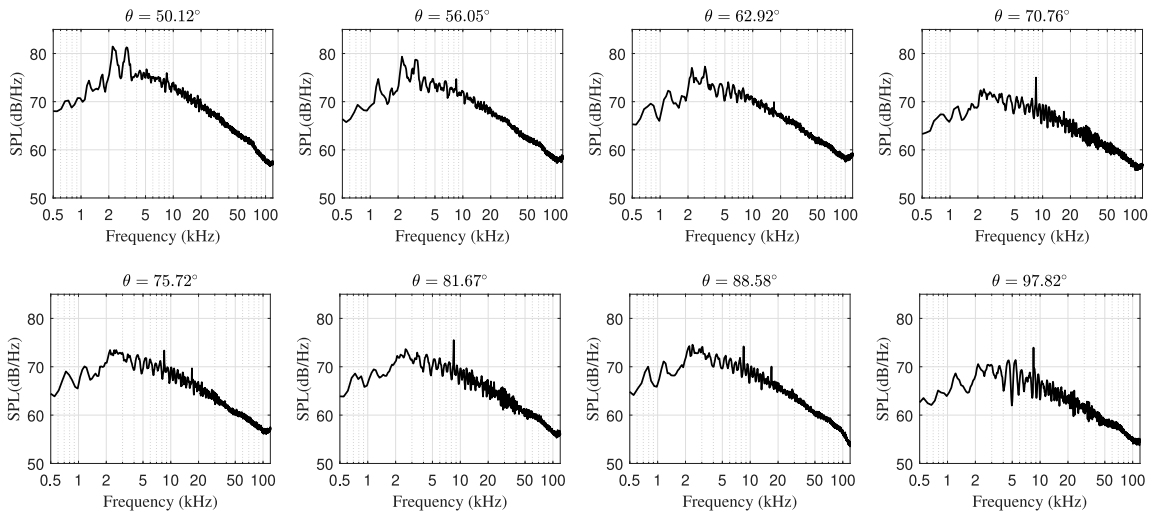


Fig. 13 SPL spectra for the isolated jet at various polar angles.

It is useful to examine the source distributions of Fig. 14 for the high frequencies, as presented in Fig. 15. It is seen how the noise source map is sharper and practically devoid of sidelobes when using the improved signal division. The dense block distribution at the high frequencies increases the number of small distances between microphone pairs and translates into higher spatial resolution. The DAS map is not included since it does not provide useful information at the high frequencies.

B. Jet with Installation Effects

Figure 16 plots the SPL spectra the isolated jet and the jet with plate in the shielding configuration ($L = 101.6$ mm = $4.7D$), measured with the fixed microphones only, for various polar angles θ . As noted in earlier works [16], in the shielding configuration the plate suppresses sound at high frequency but amplifies sound at low frequency. Within the range of the measurements, a peak reduction of ~ 8 dB is achieved at $\theta = 97.8^\circ$ and at a frequency of around 100 kHz. The stronger shielding at the high frequencies relates to the noise source location moving closer to the nozzle exit plane, as seen in the noise source maps of the isolated jet in Fig. 14. However, the peak source location at low frequencies extends up to $7-8D$ downstream of the nozzle exit plane thus is not effectively shielded, In addition, sound scattered from the plate trailing edge can overwhelm the acoustic field of the isolated jet at large polar angle, which explains the spectral rise at low frequency. Figure 17 presents similar results for L extended to 127 mm ($5.8D$). Expectedly, the shielding becomes stronger, reaching around 11 dB achieved at $\theta = 97.8^\circ$ and 100 kHz; amplification at low

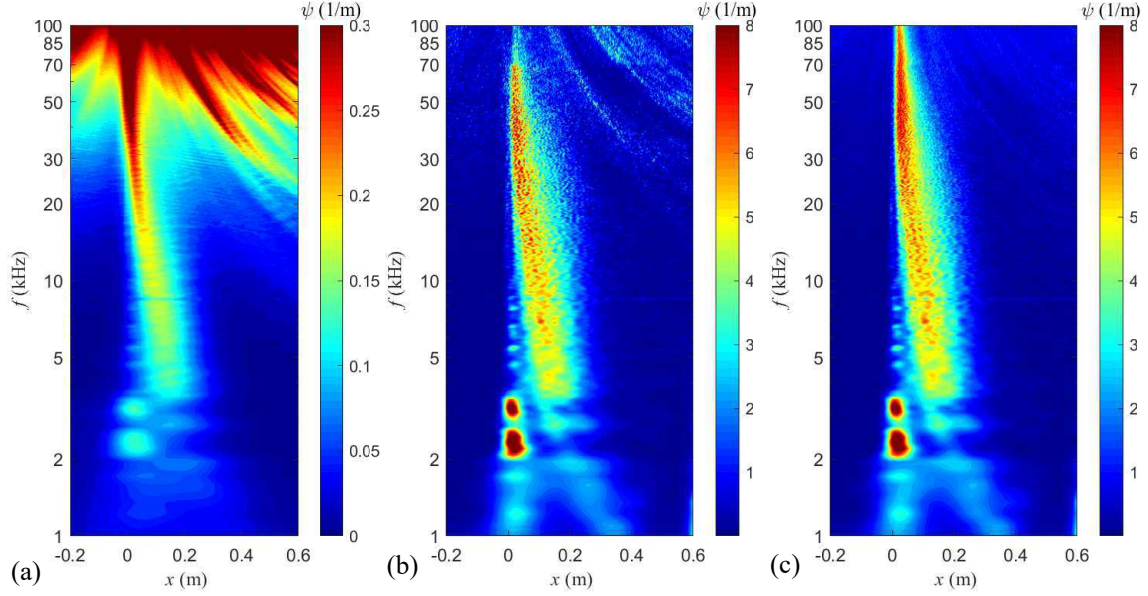


Fig. 14 Coherence-based noise source distribution $\psi(x, \omega)$ for the isolated jet. (a) DAS; (b) DSE; (c) DSEV.

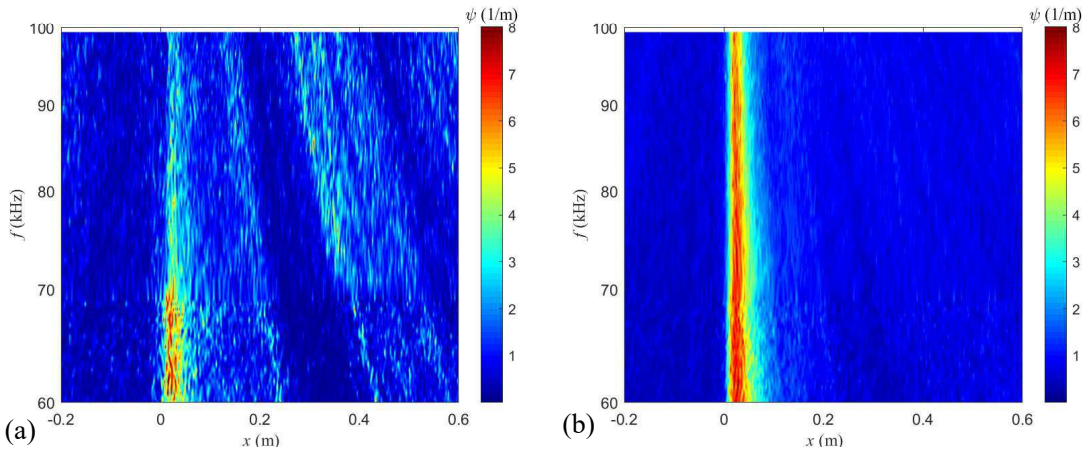


Fig. 15 Detail of the coherence-based source strength $\psi(x, \omega)$ for the isolated jet at high frequencies. (a) DSE; (b) DSEV.

frequency is moderately enhanced compared to $L = 101.6$ mm.

Figure 18 presents three coherence-based noise source maps for the jet with shielding ($L = 101.6$ mm), analogous to those of the isolated jet in Fig. 14. The DAS map suffers from strong sidelobes as in the isolated case. Although the noise source might be correctly localized, little usable information is extracted for frequencies higher than 30 kHz. The DSE map shows a clear improvement when compared to DAS: the sidelobes are strongly suppressed and the spatial resolution is enhanced, especially at the high frequencies. The DSEV method results in a map of higher quality; while the spatial resolution at low frequencies (up to 30 kHz) is comparable to that obtained with the DSE method, there is clear improvement at high frequencies. The frequencies resolved are extended up to 100 kHz, compared to around 85 kHz with the DSE. The DSEV map is practically devoid of sidelobes and the source becomes more continuous for all frequencies. The low frequency noise sources become more intense when compared to the isolated jet. This is also seen in Refs. [15, 16]. Noise from the trailing edge is evident at low frequency. Focusing on the high frequencies, Fig. 19 shows that the noise source map becomes sharper and practically devoid of sidelobes when using the improved

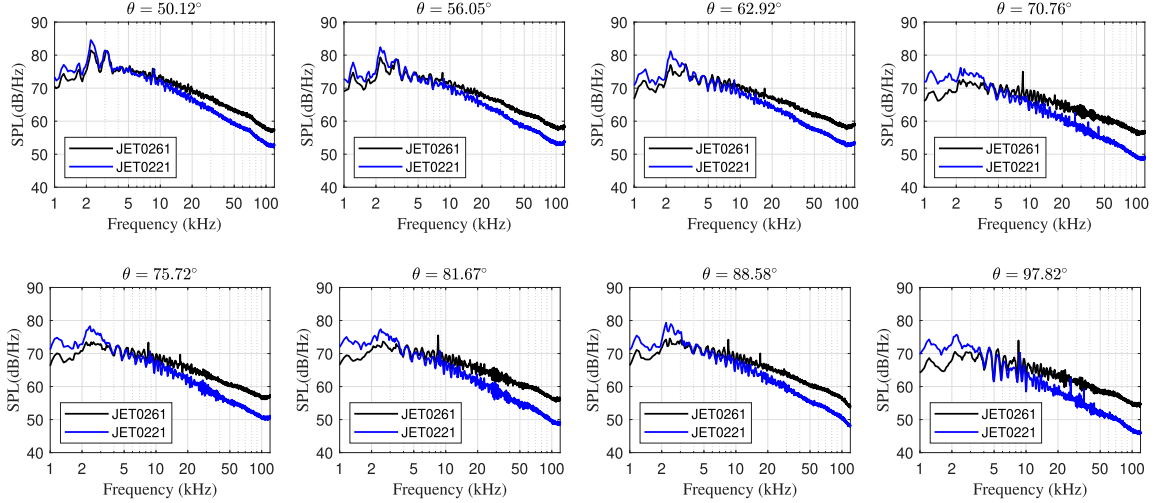


Fig. 16 SPL spectra for the isolated (black lines) and shielded (blue lines) jet at various polar angles. Plate trailing edge at $L = 101.6\text{mm}$.

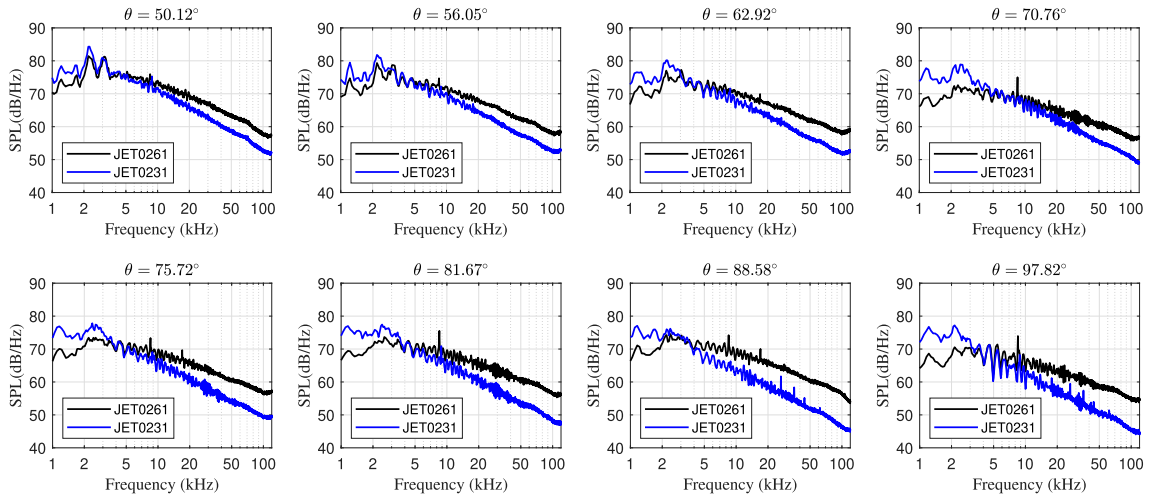


Fig. 17 SPL spectra for the isolated (black lines) and shielded (blue lines) jet at various polar angles. Plate trailing edge at $L = 127.0\text{mm}$.

signal division. Finally, Fig. 20 compares DSEV maps for the isolated jet and the jet with the shielding plate at $L = 101.6\text{ mm}$ and 127.0 mm . With the plate, the spatial distribution of the acoustic source becomes more confined at low frequency, suggesting the dominance of sound scattered by the trailing edge.

C. Jet with Reflection Plate

Figures 21 and 22 plot the SPL spectra for the isolated jet and jet with plate in the reflection configuration with $L = 101.6\text{ mm}$ and 127.0 mm , respectively. The reflection causes a significant spectral increase at low frequency and modest increase at high frequency. The trends are generally in line with previous works (e.g., Ref. [15]). Figure 23 presents noise source maps in analogy with Fig. 18. The same general observations apply as in the shielding maps, with DSEV showing clear improvement in resolving the source at high frequency and suppressing the sidelobes. Comparison of the maps in Fig. 25 indicates that the reflection affects modestly the distribution of the coherence-based noise source at high frequency, but causes a concentration of the source near the trailing edge at low frequency. The latter observation

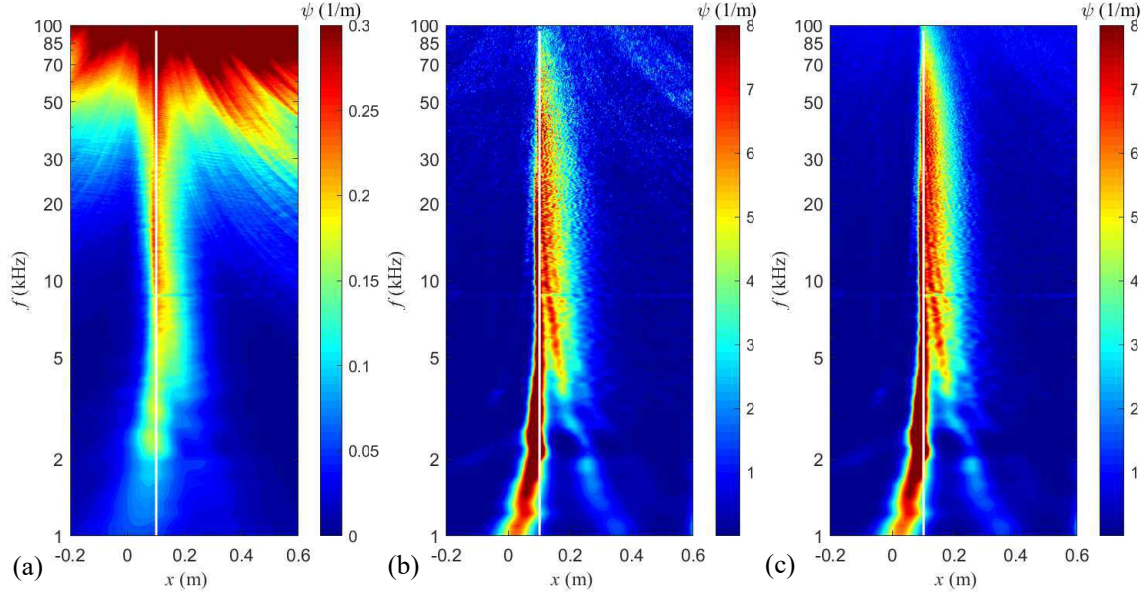


Fig. 18 Coherence-based source distribution $\psi(x, \omega)$ for the jet with plate in shielding configuration with $L = 101.6$ mm (white vertical lines). (a) DAS; (b) DSE; (c) DSEV.

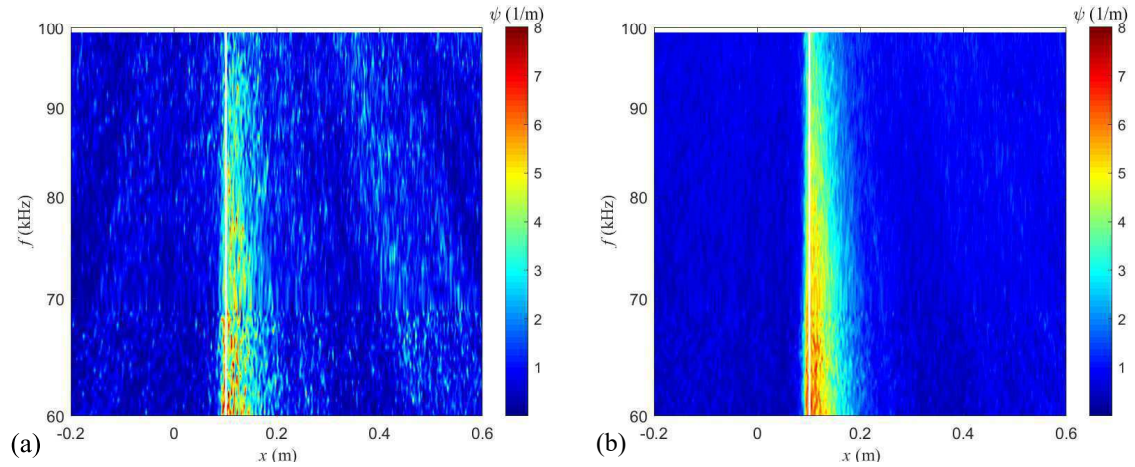


Fig. 19 High-frequency portion of the coherence-based source distribution $\psi(x, \omega)$ for the jet with plate in shielding configuration with $L = 101.6$ mm (white vertical lines). (a) DSE; (b) DSEV.

again suggests the dominance of scattering from the trailing edge at low frequency.

D. Imaging with a Sparse Array

The continuous-scan paradigm has been shown to improve the spatial resolution of the noise source when using sparse microphone arrays [5]. This section evaluates the performance of the proposed signal division on the resulting noise source maps using the sparse array of Fig. 9b. A total of 5 microphones are used; 5 fixed microphones DAS; 4 fixed and one scanning microphones for DSE and DSEV. The noise source maps of Fig. 26 indicate the failure of DAS to provide any meaningful information and the superiority of DSEV over DSE. In particular, the DSEV is able to resolve the noise source map at frequency up to 100 kHz, while DSE can only resolve up to 50 kHz. The suppression of sidelobes with DSEV is evident. This underscores how the continuous-scan approach, combined with the proposed

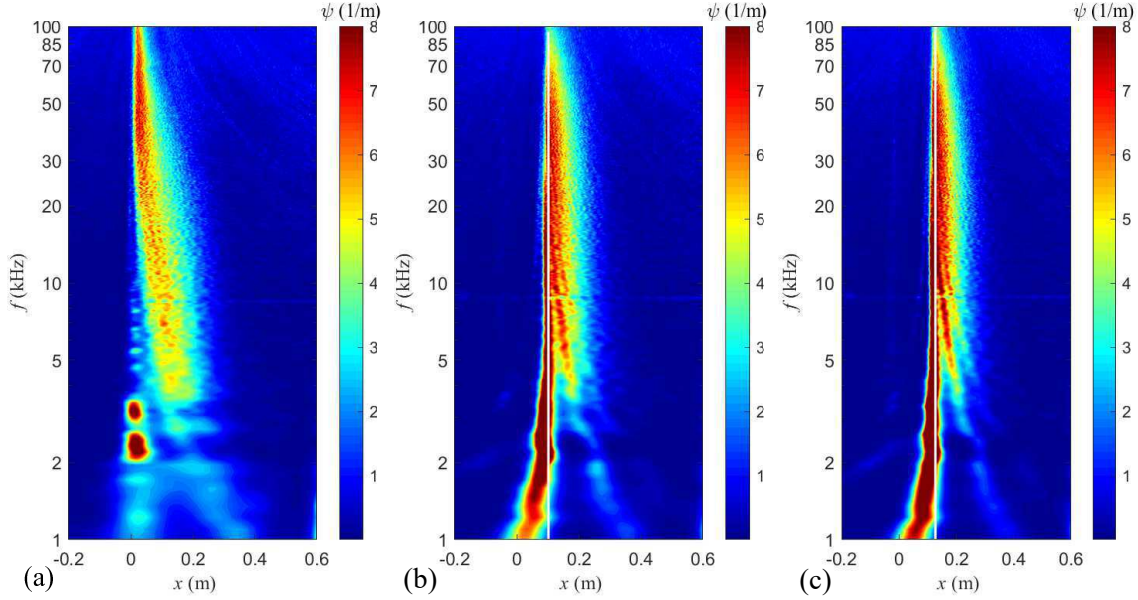


Fig. 20 DSEV maps of coherence-based source distribution $\psi(x, \omega)$. (a) Isolated jet; (b) jet with the shielding plate at $L = 101.6$ mm; (c) jet with the shielding plate at $L = 127$ mm. The white vertical lines mark the position of the trailing edge.

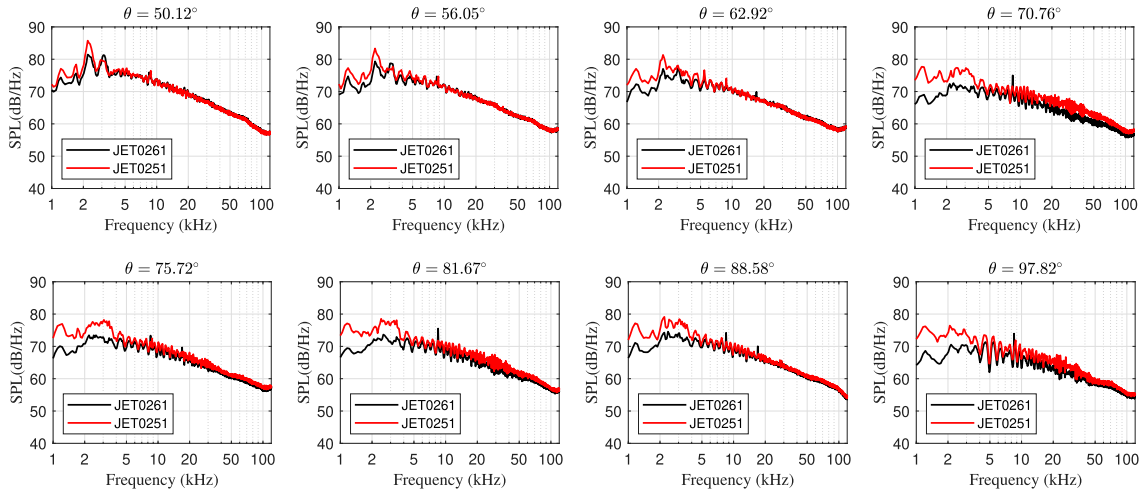


Fig. 21 SPL spectra for the isolated (black lines) and reflected (red lines) jet at various polar angles. Plate trailing edge at $L = 101.6$ mm.

signal segmentation, can provide very high quality noise source images even when using microphone arrays with a small number of sensors. The proposed signal division increases the number of small distances between microphone pairs, particularly for high frequencies, which translates into a reduced aliasing effect and a finer spatial resolution.

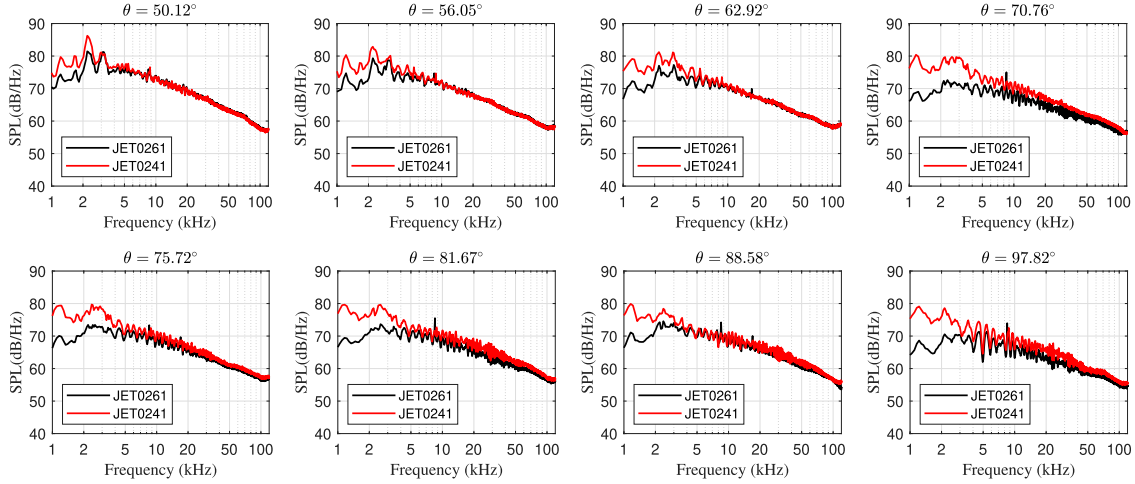


Fig. 22 SPL spectra for the isolated (black lines) and reflected (red lines) jet at various polar angles. Plate trailing edge at $L = 127.0\text{mm}$.

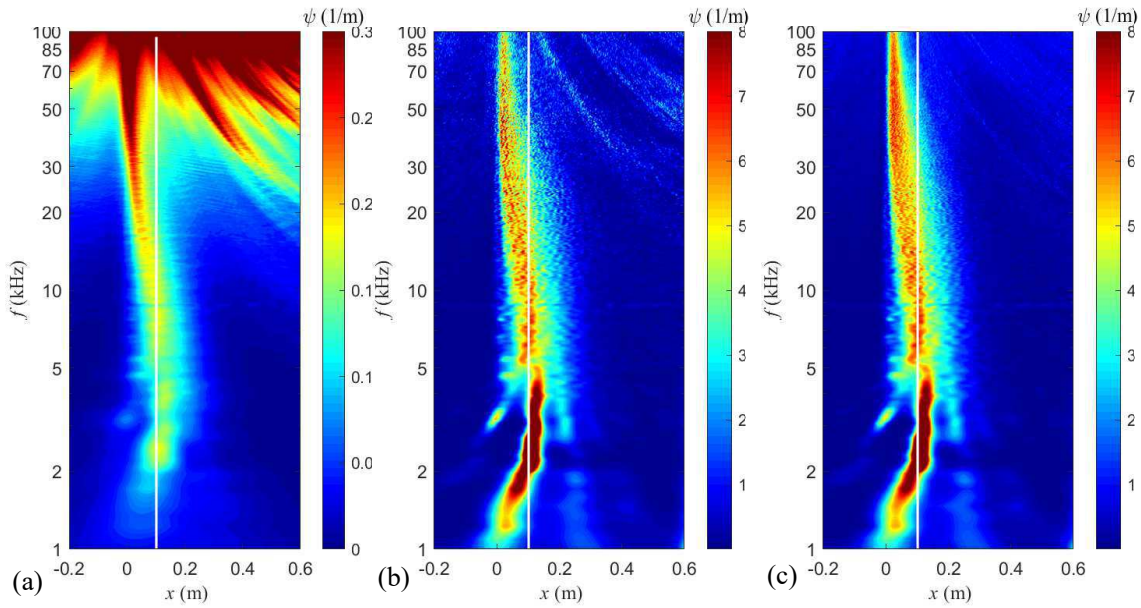


Fig. 23 Coherence-based source distribution $\psi(x, \omega)$ for the jet with plate in reflection configuration with $L = 101.6\text{ mm}$ (white vertical lines). (a) DAS; (b) DSE; (c) DSEV.

VI. Conclusions

This study introduced improvements to the methodology for the direct estimation of the spatio-spectral distribution of an acoustic source from microphone measurements that comprise fixed and continuously scanning sensors. The signals from the scanning sensors are non-stationary due to the time-varying source-sensor distance and the traversing of an acoustic field with spatially varying statistics. Quasi-stationarity is sought by dividing the signals into blocks and applying of a frequency-dependent window within each block. Geometric effects, spatial resolution, spectral accuracy, and adequacy of samples within each block are considered in the formulation of criteria for optimal block size and block overlap within frequency ranges. Implementation of the method entails discrete reductions in block size and Fourier-transform size with increasing frequency. The end result entails patching of the maps obtained with the

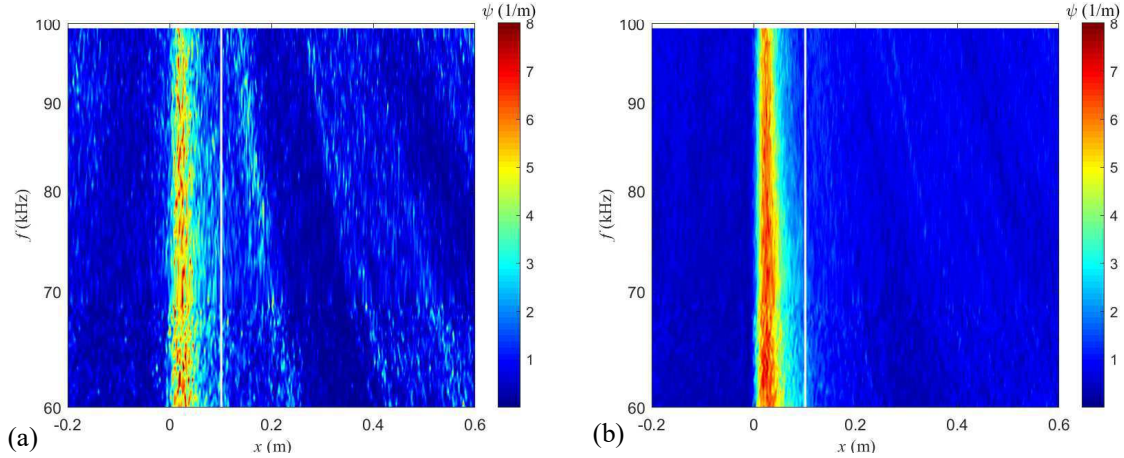


Fig. 24 High-frequency portion of the coherence-based source distribution $\psi(x, \omega)$ for the jet with plate in reflection configuration with $L = 101.6$ mm (white vertical lines). (a) DSE; (b) DSEV.

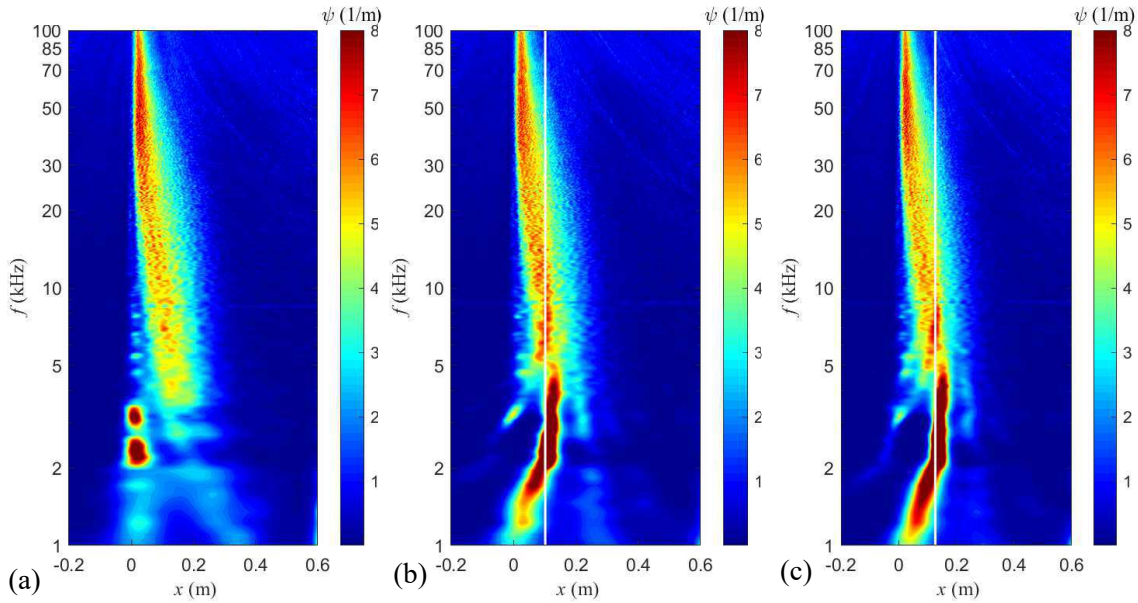


Fig. 25 DSEV maps of coherence-based source distribution $\psi(x, \omega)$. (a) Isolated jet; (b) jet with the reflection plate at $L = 101.6$ mm; (c) jet with the reflection plate at $L = 127$ mm. The white vertical lines mark the position of the trailing edge.

variable-sized blocks.

The methodology was applied to the acoustic field emitted by a subsonic jet in isolation and surrounded by a rectangular plate in shielding and reflection orientations. The nominal measurement setup comprised one continuously scanning microphone and 23 fixed microphones. Noise source maps obtained with the variable-block-size approach show clear improvement over those obtained with a constant block size : increased spatial resolution and practical elimination of sidelobes. The maximum resolved frequency is increased by a factor of 1.2. The ability of the method to generate high-quality noise source maps was further demonstrated in an array comprising only four fixed sensors.

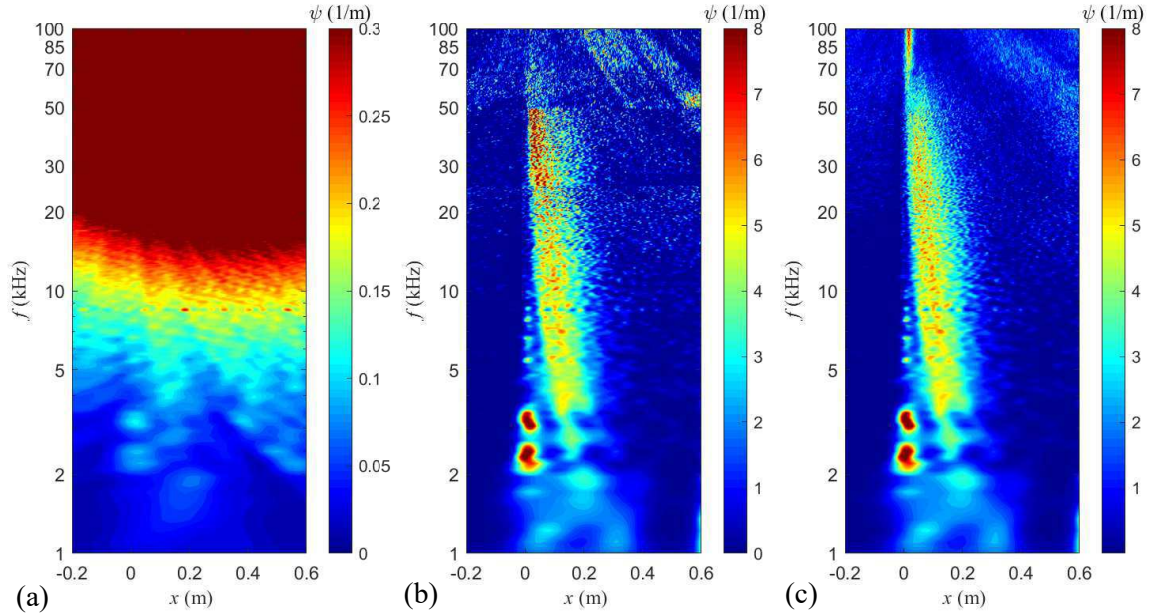


Fig. 26 Coherence based source strength $\psi(x, \omega)$ for the isolated jet. (a) Delay-and-sum with 5 fixed microphones; (b) DSE with 4 fixed sensors and 1 scanning sensor; (c) DSEV with 4 fixed sensors and 1 scanning sensor.

Acknowledgment

This work was conducted with NASA Phase I and Phase II Small Business Innovation Research (SBIR) funding (contracts NNX16CC79P and NNX17CC18C) under Technical Monitor David Stephens. Partial support for D. Morata came from a Balsells Fellowship.

References

- [1] Brooks, T. F., and Humphreys, W. M., “A deconvolution approach for the mapping of acoustic sources (DAMAS) determined from phased microphone arrays,” *Journal of Sound and Vibration*, Vol. 294, No. 4, 2006, pp. 856 – 879. doi:10.1016/j.jsv.2005.12.046.
- [2] Dougherty, R., “Extensions of DAMAS and Benefits and Limitations of Deconvolution in Beamforming,” *AIAA Paper 2005-2961*, 2005. doi:10.2514/6.2005-2961.
- [3] Sijtsma, P., “CLEAN Based on Spatial Source Coherence,” *International Journal of Aeroacoustics*, Vol. 6, No. 4, 2007, pp. 357–374. doi:10.1260/147547207783359459.
- [4] Papamoschou, D., “Imaging of Distributed Directional Noise Sources,” *Journal of Sound and Vibration*, Vol. 330, No. 10, 2011, pp. 2265–2280. doi:10.1016/j.jsv.2010.11.025.
- [5] Papamoschou, D., Morata, D., and Shah, P., “Inverse Acoustic Methodology for Continuous-Scan Phased Arrays,” *AIAA Journal*, Vol. 57, No. 12, 2019, pp. 5126–5141. doi:10.2514/1.J058085.
- [6] Leclère, Q., Pereira, A., Bailly, C., Antoni, J., and Picard, C., “A unified formalism for acoustic imaging based on microphone array measurements,” *International Journal of Aeroacoustics*, Vol. 16, No. 4-5, 2017, pp. 431–456. doi:10.1177/1475472X17718883.
- [7] Pereira, A., Antoni, J., and Leclère, Q., “Empirical Bayesian regularization of the inverse acoustic problem,” *Applied Acoustics*, Vol. 97, 2015, pp. 11–29. doi:10.1016/j.apacoust.2015.03.008.
- [8] Shah, P. N., and Papamoschou, D., “Characterization of High Speed Jet Acoustics Using High-resolution Multi-reference Continuous-scan Acoustic Measurements on a Linear Array,” *AIAA Paper 2020-0005*, 2020. doi:10.2514/6.2020-0005.

- [9] Vold, H., Shah, P., Davis, J., Bremner, P., McLaughlin, D., Morris, P., Veltin, J., and McKinley, R., “High Resolution Continuous Scan Acoustical Holography Applied to High-Speed Jet Noise,” *AIAA Paper 2010-3754*, 2010. doi:10.2514/6.2010-3754.
- [10] Shah, P., Vold, H., and Yang, M., “Reconstruction of Far-Field Noise Using Multireference Acoustical Holography Measurements of High-Speed Jets,” 2011. doi:10.2514/6.2011-2772.
- [11] Stephens, D. B., and Vold, H., “Order tracking signal processing for open rotor acoustics,” *Journal of Sound and Vibration*, Vol. 333, No. 16, 2014, pp. 3818 – 3830. doi:https://doi.org/10.1016/j.jsv.2014.04.005.
- [12] Comesaña, D. F., Holland, K. R., Escibano, D. G., and de Bree, H.-E., “An Introduction to Virtual Phased Arrays for Beamforming Applications,” *Archives of Acoustics*, Vol. 39, 2014, pp. 81–88. doi:10.2478/aoa-2014-0009.
- [13] Papamoschou, D., and Rostamimonjezi, S., “Effect of Velocity Ratio on Noise Source Distribution of Coaxial Jets,” *AIAA Journal*, Vol. 48, No. 7, 2010, pp. 1504–1512. doi:10.2514/1.J050140.
- [14] Von Glahn, U., and Goodykoontz, J., “Forward Velocity Effects on Jet Noise with Dominant Internal Noise Source,” *The Journal of the Acoustical Society of America*, Vol. 55, No. 2, 1974, pp. 438–438. doi:10.1121/1.3437412.
- [15] Podboy, G., “Jet-Surface Interaction Test: Phased Array Noise Source Localization Results,” *ASME Paper GT2012-69801*, 2012, pp. 381–414. doi:10.1115/GT2012-69801.
- [16] Papamoschou, D., “Prediction of Jet Noise Shielding,” *AIAA Paper 2010-0653*, 2010. doi:10.2514/6.2010-653.